



Cite this: *RSC Adv.*, 2017, 7, 38526

# Structures, stabilities and spectral properties of metalloborospherenes $MB_{40}^{0/-}$ ( $M = Cu, Ag, \text{ and } Au$ )<sup>†</sup>

Shi-Xiong Li,<sup>a</sup> Zheng-Ping Zhang,<sup>\*ab</sup> Zheng-Wen Long<sup>c</sup> and Shui-Jie Qin<sup>d</sup>

The discovery of borospherene  $B_{40}$  marks the onset of a new class of boron fullerenes and it is of current interest in chemical physics and, in particular, boron chemistry. In this work, density functional theory (DFT) and time-dependent density functional theory (TD-DFT) calculations are carried out to study the structures, stabilities, photoelectron spectra, infrared spectra, Raman spectra and electronic absorption spectra of metalloborospherenes  $MB_{40}^{0/-}$  ( $M = Cu, Ag, \text{ and } Au$ ). It is found that Cu, Ag and Au atoms can form stable exohedral metalloborospherenes  $M\&B_{40}^{0/-}$  ( $M = Cu, Ag, \text{ and } Au$ ) and endohedral metalloborospherenes  $M@B_{40}^{0/-}$  ( $M = Cu, Ag, \text{ and } Au$ ). In addition, the relative energies of these metalloborospherenes suggest that Cu, Ag and Au atoms favor the exohedral configuration. The Cu atom favors an exohedral geometry with the dopant face-capping a heptagon on the side surface ( $\eta^7\text{-Cu}$ ), whereas Ag and Au atoms favor exohedral geometries with the dopant bonding a side boron atom of the hexagonal ring. The calculated spectra suggest that doping of metal atoms in borospherene  $B_{40}$  can change the spectral features since the extra metal atoms can modify the electronic structure of borospherene  $B_{40}$ . The addition of metal atoms can lead to more infrared and Raman active modes and redshift the electronic absorption spectra. The calculated results also show that metalloborospherenes  $MB_{40}^{0/-}$  ( $M = Cu, Ag, \text{ and } Au$ ) have different and meaningful spectral features, insight into the spectral properties is important to understand the compounds and reveal their potential applications. These spectral features can be readily compared with future spectroscopy measurements and used as fingerprints to identify and distinguish the metalloborospherenes  $MB_{40}^{0/-}$  ( $M = Cu, Ag, \text{ and } Au$ ).

Received 26th May 2017

Accepted 27th July 2017

DOI: 10.1039/c7ra05932a

rsc.li/rsc-advances

## Introduction

Since the discovery of  $C_{60}$ ,<sup>1</sup> boron clusters have been received ample attention and previous works have shown that most boron clusters are planar or quasi-planar structures.<sup>2-9</sup> In addition, stuffed fullerene-like boron carbide nanoclusters, boron sheets and different three-dimensional (bowl, tube, cage) boron clusters have been proposed based on theoretical calculations.<sup>10-22</sup> Exhilaratingly, an all-boron fullerene  $B_{40}^-$  was produced using a laser vaporization supersonic source in 2014.<sup>23</sup> Photoelectron spectroscopy analysis confirmed the existence of  $B_{40}^-$ . The first all-boron fullerene with 40 atoms is named 'borospherene'. Soon after, the all-boron fullerene  $B_{39}^-$  was also produced *via* laser vaporization.<sup>24</sup> The first observation of borospherene has aroused interest in boron clusters and

their derivatives such as the dynamic behavior of  $B_{40}$ ,<sup>25</sup> hydrogen storage capacity of Ti-decorated  $B_{40}$ ,<sup>26</sup> manganese-centered and cobalt-centred tubular boron clusters ( $MnB_{16}^-$  and  $CoB_{16}^-$ ),<sup>27,28</sup> experimental and theoretical studies of  $B_n^-$  ( $n = 27-29$ ),<sup>29-31</sup> structures and properties of borospherenes ( $B_{42}^+$ ,  $B_{44}^{0/-}$ , and  $B_{46}$ ),<sup>32-35</sup> structures of boron clusters  $B_n$  ( $n = 30$  to 51) and exohedral complexation in  $C_6H_6CrB_{40}$ ,<sup>36,37</sup>  $CO_2$  capture, storage and separation by borospherene  $B_{40}$ ,<sup>38</sup> and spectral properties of borospherenes  $B_{40}^{0/-}$ .<sup>39,40</sup>

Since the discovery of fullerene  $C_{60}$ ,<sup>1</sup> researchers have reported the development of several fullerene derivatives based on the functionalization of the  $C_{60}$  aiming to produce new properties or improve their existing properties. The important studies involve the use of  $C_{60}$  derivatives in biological systems,<sup>41,42</sup> solar cells<sup>43,44</sup> and superconductors.<sup>45</sup> Endofullerenes based on  $C_{60}$  have attracted much attention due their potential applications in superconductivity and materials science.<sup>46-49</sup> Similarly, can metalloborospherenes also show new properties? Several theoretical studies have been reported to investigate the structures and electronic properties of metalloborospherenes.<sup>50-57</sup> Bai *et al.* reported the metalloborospherenes  $MB_{40}$  ( $M = Ca, Mg, Sr, \text{ and } Be$ ), they found that both Ca and Sr with bigger atomic radii exhibit endohedral structures as the global minima, whereas Be and Mg with smaller atomic radii favor the exohedral geometries with the

<sup>a</sup>School of Physics and Electronic Science, Guizhou Education University, Guiyang 550018, China. E-mail: leesoptics@163.com

<sup>b</sup>College of Big Data and Information Engineering, Guizhou University, Guiyang 550025, China. E-mail: zpzhang@gzu.edu.cn

<sup>c</sup>College of Physics, Guizhou University, Guiyang 550025, China

<sup>d</sup>Key Lab of Photoelectron Technology and Application, Guizhou University, Guiyang 550025, China

<sup>†</sup> Electronic supplementary information (ESI) available. See DOI: 10.1039/c7ra05932a



dopant face-capping a heptagon on the side surface ( $\eta^7$ -M). Their studies suggest that the atomic radii of metal dopants play a key factor in determining stability of the metalloborospherenes. Jin *et al.* reported the metalloborospherenes MB<sub>40</sub> (M = Sc, Y, and La). They found that Sc, Y, and La atoms all favor the off-center location within the B<sub>40</sub> cage. However, in another study of metalloborospherenes MB<sub>40</sub> (M = Li, Na, Ba, and K), the results show that K favors the  $\eta^7$ -K exohedral location whereas Na favors the endohedral off-center location, even though the size of Na (1.91 Å) is smaller than that of K (2.34 Å). So the atomic radius of metal dopant is not the only factor in determining stability of the metalloborospherenes. Therefore, it will be useful to determine additional factors that can be used to identify the preference of endohedral or exohedral doping for the metal atoms. It is necessary to examine all possible binding configurations of other metal atoms with the B<sub>40</sub> cage.

Ag and Au have often been used as electrodes of single-molecule device, such as the electrical transport properties of single-molecule devices Au-B<sub>40</sub>-Au and Au-Sr@B<sub>40</sub>-Au were studied by using density functional theory and non-equilibrium Green's function method.<sup>58-60</sup> It is necessary to investigate the structures and stabilities of metalloborospherenes MB<sub>40</sub><sup>0/-</sup> (M = Ag, Au). On the one hand, it can enrich the research of metalloborospherenes, on the other hand, it also can provide theoretical guidance for borospherene or metalloborospherene molecular devices. In this work, we provide a theoretical study on the structures, stabilities, photoelectron spectra, infrared, Raman and electronic absorption spectra of metalloborospherenes MB<sub>40</sub><sup>0/-</sup> (M = Cu, Ag, and Au). Our works can provide valuable results to assist further experimental identifications on the metalloborospherenes MB<sub>40</sub><sup>0/-</sup> (M = Cu, Ag, and Au), and also may provide theoretical guidance for the applications and synthesis of them in the future.

## Computational methods

To gain relative stabilities between the endohedral and exohedral structures of metalloborospherenes MB<sub>40</sub><sup>0/-</sup> (M = Cu, Ag, and Au), we divided into two steps. First, we performed a scan of potential energy by using the dopant as a probe to move along the path connecting the B<sub>40</sub> center toward the outside but keeping the B<sub>40</sub> cage intact. Considering the molecular symmetry ( $D_{2d}$ ), six target paths were selected. (1) L<sub>y</sub>: connecting the B<sub>40</sub> center and a heptagon center (y axis); (2) L<sub>z</sub>: connecting the B<sub>40</sub> center and a hexagon center (z axis); (3) L<sub>xy</sub>: angle bisector of angle between x axis and y axis; (4) L<sub>yz</sub>: angle bisector of angle between y axis and z axis; (5) L<sub>xz</sub>: angle bisector of angle between x axis and z axis; (6) L<sub>xyz</sub>: intersection line of three planes determined by x axis and L<sub>yz</sub>, z axis and L<sub>xz</sub>, y axis and L<sub>xz</sub>, respectively. Structure of  $D_{2d}$  B<sub>40</sub> indicates that there exist six kinds of boron atoms with different chemical environment (confirmed by the NBO charge analysis and calculated <sup>11</sup>B NMR spectrum<sup>61,62</sup>), two of which belong to hexagon and four to heptagon as shown by different numbers in Fig. 1. Four paths containing L<sub>xz</sub>, L<sub>xy</sub>, L<sub>yz</sub> and L<sub>xyz</sub> ensure the dopant atop six different boron atoms. This method is a quick and advisable computational indicator to demonstrate the relative stabilities

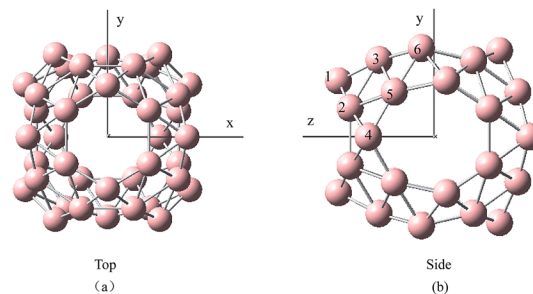


Fig. 1 Structures of B<sub>40</sub><sup>0/-</sup> observed along the (a) z direction and (b) x direction. Six numbers denote the six kinds of boron atoms with different chemical environment.

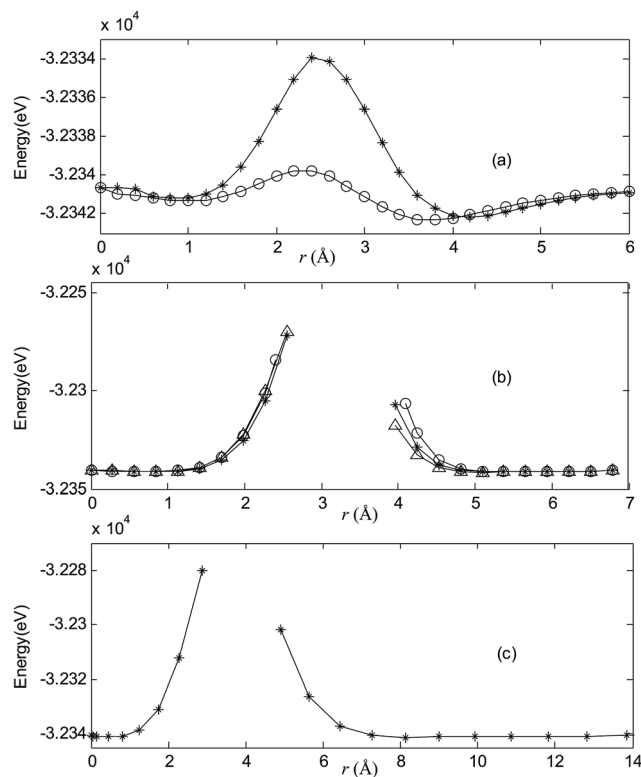
between the endohedral and exohedral configurations of metallofullerenes and metalloborospherenes.<sup>52,63</sup> In the last step, geometry optimizations and frequency calculations were performed containing local minima in the six target paths. The potential energy scan was performed using the PBE0 functional with 6-31G basis set for boron and a double- $\zeta$  basis set (LanL2DZ) with the effective core potential for metals. Geometry optimizations and harmonic frequency analysis were carried out using the PBE0 functional with 6-311+G\* basis set for boron and a double- $\zeta$  basis set (LanL2DZ) with the effective core potential for metals. These optimized structures were then used in the calculations of photoelectron spectra and electronic absorption spectra based on the time-dependent DFT formalism.<sup>64</sup> Adiabatic detachment energy (ADE) was calculated as the energy difference of the anion and neutral metalloborospherenes at their respective optimized geometries. The first vertical detachment energy (VDE) was calculated as the energy difference between the anion ground state and the neutral at the optimized anion geometry. The higher vertical detachment energies (VDEs) were approximated *via*  $\Delta$ SCF-time-dependent density functional theory ( $\Delta$ SCF-TD-DFT).<sup>23,24,64</sup> All computations were carried out using the Gaussian09 software package.<sup>65</sup>

## Results and discussion

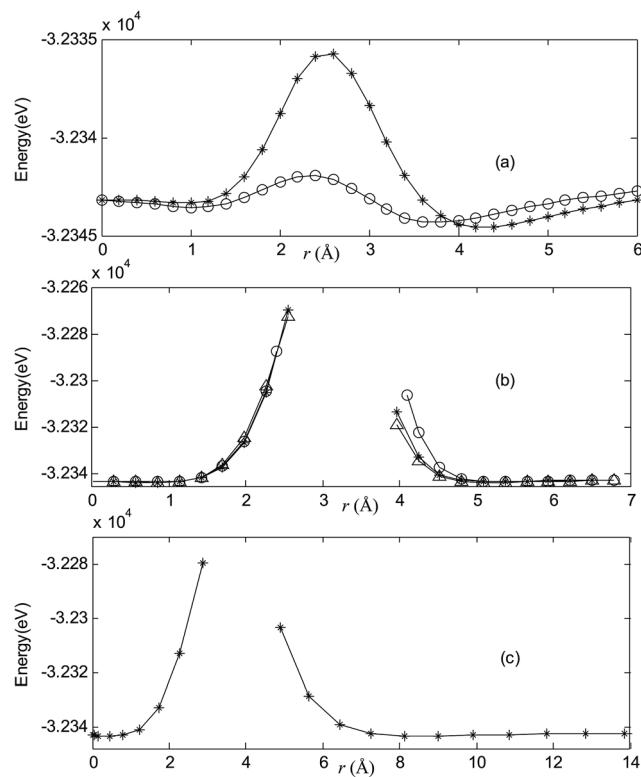
### Structures

Fig. 2–7 are results of potential energy scan by moving the metal dopant from the cage center through different paths while keeping the cage intact. The open location of each curve is just cage surface in the presence of boron atoms. The results indicate that these potential energy curves exhibit two local minima: one corresponds to the endohedral structure, whereas another corresponds to the exohedral structure. We also notice that the exohedral minimum is lower in energy than the endohedral minimum. For endohedral Ag@B<sub>40</sub>, Ag@B<sub>40</sub><sup>-</sup> and Au@B<sub>40</sub>, when the dopant is at the center of cage, endohedral structure is local minimum. However, for both Cu@B<sub>40</sub> and Cu@B<sub>40</sub><sup>-</sup>, endohedral structure which the dopant is at the off-center location within the cage is local minimum. In addition, endohedral Au@B<sub>40</sub><sup>-</sup> which the dopant is at the slightly off-center location within the cage is local minimum.





**Fig. 2** Potential energy scan by moving the metal dopant Cu from the cage center through different paths while keeping the cage intact for  $\text{CuB}_{40}$ .  $r$  represents the distance between the dopant Cu and the cage center. (a) Asterisk represents the path  $L_z$ , circle represents the path  $L_y$ , (b) triangle represents the path  $L_{yz}$ , asterisk represents the path  $L_{xz}$ , circle represents the path  $L_{xz}$ , (c) the path  $L_{xyz}$ .



**Fig. 3** Potential energy scan by moving the metal dopant Cu from the cage center through different paths while keeping the cage intact for  $\text{CuB}_{40}^-$ .  $r$  represents the distance between the dopant Cu and the cage center. (a) Asterisk represents the path  $L_z$ , circle represents the path  $L_y$ , (b) triangle represents the path  $L_{yz}$ , asterisk represents the path  $L_{xz}$ , circle represents the path  $L_{xz}$ , (c) the path  $L_{xyz}$ .

For all metalloborospherenes  $\text{MB}_{40}^{0/-}$  ( $M = \text{Cu}, \text{Ag}, \text{and Au}$ ), as illustrated in Fig. 2–7, the energy rapidly increases near the cage surface and exhibits a maximum at the cage surface. In addition, the energy rapidly increases near the hexagonal and heptagonal rings and exhibits a maximum at the center of the hexagonal and heptagonal ring, respectively. The energy barriers for the Cu, Ag, and Au dopants are 1.54 eV ( $\text{CuB}_{40}$ ), 1.61 eV ( $\text{CuB}_{40}^-$ ), 7.72 eV ( $\text{AgB}_{40}$ ), 7.92 eV ( $\text{AgB}_{40}^-$ ), 7.55 eV ( $\text{AuB}_{40}$ ), and 7.29 eV ( $\text{AuB}_{40}^-$ ) for their moving “in” through the heptagon ring, respectively. The energy barriers for the  $\text{CuB}_{40}^{0/-}$ ,  $\text{AgB}_{40}^{0/-}$ , and  $\text{AuB}_{40}^{0/-}$  dopants are 7.18 eV ( $\text{CuB}_{40}$ ), 7.70 eV ( $\text{CuB}_{40}^-$ ), 19.09 eV ( $\text{AgB}_{40}$ ), 20.27 eV ( $\text{AgB}_{40}^-$ ), 20.98 eV ( $\text{AuB}_{40}$ ), 21.79 eV ( $\text{AuB}_{40}^-$ ) for their moving “in” through the hexagon ring, respectively. The larger the ionic radius, the higher is the energy barrier. The large barrier height found for Ag and Au indicates that the atom cannot escape from  $\text{B}_{40}$  once encapsulated. In addition, for a dopant, the energy barrier is smaller for the heptagon ring, indicating stronger interaction for the hexagon ring. The results can be understood by comparing the size of the hexagonal and heptagonal ring.<sup>63</sup> The hexagonal ring radius is smaller compared with the heptagonal ring radius, but smaller radius leads to stronger interaction to pass through the hexagonal ring with closer touching the electrons responsible for the B–B bond. The heptagonal ring radius is already larger

than the hexagonal ring radius, where the energy barrier is smaller for heptagonal ring.

The above results indicate that the exohedral minimum is lower in energy than the endohedral minimum. To gain the further understanding of relative stabilities between the endohedral and exohedral structures of metalloborospherenes  $\text{MB}_{40}^{0/-}$  ( $M = \text{Cu}, \text{Ag}, \text{and Au}$ ), geometry optimizations and frequency calculations were performed for the two local minima in the six paths. Optimized structures of metalloborospherenes  $\text{MB}_{40}^{0/-}$  ( $M = \text{Cu}, \text{Ag}, \text{and Au}$ ) are depicted in Fig. S1–S3 (ESI†). Relative energy values of neutral and corresponding anionic metalloborospherenes  $\text{MB}_{40}^{0/-}$  indicate that the exohedral minimum is lower in energy than the endohedral minimum. The results also reveal that Cu, Ag and Au atoms favor the exohedral configuration. For neutral and anionic metalloborospherenes  $\text{CuB}_{40}^{0/-}$ , the isomer (see Fig. S1(a)†) with Cu capping a heptagon ( $\eta^7\text{-Cu}$ ) is lower in energy than another exohedral and endohedral isomers. The results are same with the found that  $\text{MB}_{40}$  ( $M = \text{Be}, \text{Mg}, \text{Li}, \text{and K}$ ) favor the exohedral geometries with the dopant face-capping a heptagon on the side surface ( $\eta^7\text{-M}$ ). For neutral and anionic metalloborospherenes  $\text{MB}_{40}^{0/-}$  ( $M = \text{Ag and Au}$ ), the isomer (see Fig. S2(a) or S3(a)†) with dopant bonding the side boron atom of the hexagonal ring is lower in energy than another exohedral and endohedral isomers. This isomer with  $C_s$  symmetry is predicted after the



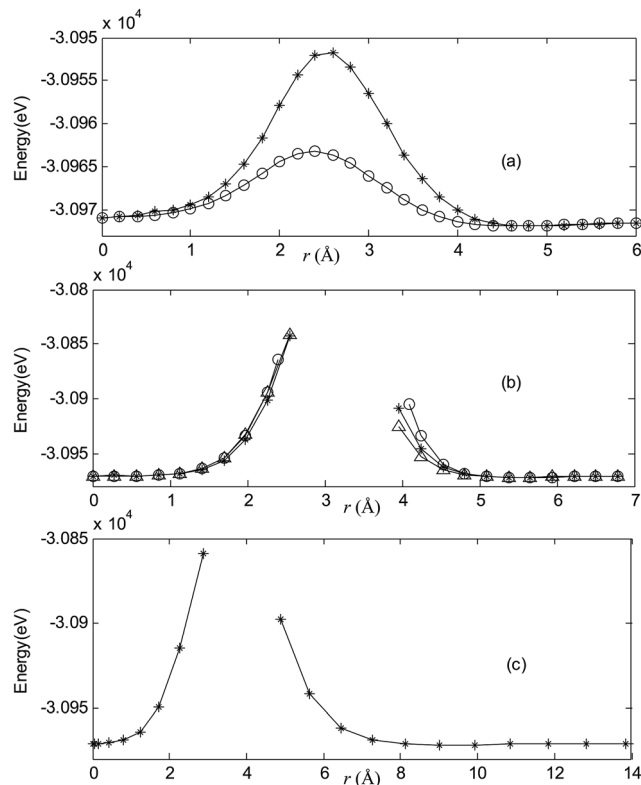


Fig. 4 Potential energy scan by moving the metal dopant Ag from the cage center through different paths while keeping the cage intact for  $\text{AgB}_{40}$ .  $r$  represents the distance between the dopant Ag and the cage center. (a) Asterisk represents the path  $L_z$ , circle represents the path  $L_y$ , (b) triangle represents the path  $L_{yz}$ , asterisk represents the path  $L_{xy}$ , circle represents the path  $L_{xz}$ , (c) the path  $L_{xyz}$ .

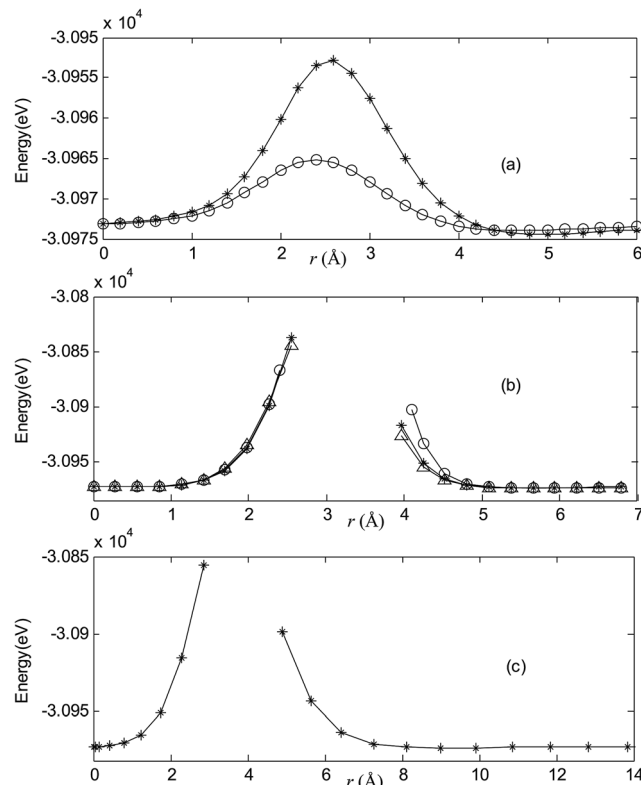


Fig. 5 Potential energy scan by moving the metal dopant Ag from the cage center through different paths while keeping the cage intact for  $\text{AgB}_{40}^-$ .  $r$  represents the distance between the dopant Ag and the cage center. (a) Asterisk represents the path  $L_z$ , circle represents the path  $L_y$ , (b) triangle represents the path  $L_{yz}$ , asterisk represents the path  $L_{xy}$ , circle represents the path  $L_{xz}$ , (c) the path  $L_{xyz}$ .

relaxation in the path  $L_{yz}$ . The result further proves the research results that single-molecule device  $\text{Au-B}_{40}\text{-Au}$  which electrode is connected to the hexagonal ring is the most stable configuration.<sup>60</sup> For most stable endohedral metalloborospherenes  $\text{M@B}_{40}^{0/-}$ , the calculated results indicate that Cu atom in  $\text{Cu@B}_{40}^-$  and  $\text{Cu@B}_{40}$  are off the molecular center and near the heptagonal ring. However, Ag atom in  $\text{Ag@B}_{40}^-$  and Au atom in  $\text{Au@B}_{40}$  are at the molecular center. In addition, Au atom in  $\text{Au@B}_{40}^-$  is slightly off the molecular center. It's worth noting that configuration of  $\text{Au@B}_{40}^-$  has obvious changes and symmetry of  $\text{Au@B}_{40}^-$  reduces to  $C_1$ . Frequency calculations confirm the stabilities of these most stable endohedral and exohedral metalloborospherenes by showing no imaginary frequencies. We will focus on the most stable endohedral and exohedral metalloborospherenes. The most stable endohedral and exohedral metalloborospherenes are depicted in Fig. 8–10, ground-state parameters are summarized in Table 1. As shown in Table 1, HOMO–LUMO energy gaps of metalloborospherenes  $\text{MB}_{40}^-$  (with closed-shell electronic structure) are smaller than HOMO–LUMO energy gap of borospherene  $\text{B}_{40}$  (3.13 eV).<sup>23</sup> It indicates that the addition of metal atom (Cu, Ag, or Au) can reduce the HOMO–LUMO energy gap and improve the chemical activity of borospherene  $\text{B}_{40}$ . In addition, dipole moments of  $\text{Ag@B}_{40}^{0/-}$  and  $\text{Au@B}_{40}$  are zero among all the

metalloborospherenes because of the highly symmetric structures ( $D_{2d}$ ), this indicates that they do not render far-infrared pure rotation spectrum. For each neutral metalloborospherene, the addition of metal with odd electrons introduces spin density into the boron framework (see Fig. S4<sup>†</sup>). For metalloborospherenes  $\text{Cu@B}_{40}$  and  $\text{Cu@B}_{40}^-$ , the spin components are mainly distributed in the surface of the cage. For metalloborospherenes  $\text{Ag@B}_{40}$  and  $\text{Au@B}_{40}$ , the spin components are mainly localized on metal and boron atoms in close proximity to metal. For metalloborospherenes  $\text{Ag@B}_{40}$  and  $\text{Au@B}_{40}$ , the spin components are mainly localized on metal (or cage centers). Especially, for metalloborospherenes  $\text{AgB}_{40}$  and  $\text{AuB}_{40}$ , the up-spin components are mainly contributed by the metal. These characteristics are expected to lead to interesting magnetic properties and potential application in metalloborospherene molecular devices.

### Photoelectron spectra

Photoelectron spectroscopy is powerful experimental technique to probe the electronic structure of cluster. It can be viewed as an electronic fingerprint for the underlying cluster. Photoelectron spectroscopy in combination with theoretical calculations has been used to understand and identify the structures of size-selected boron clusters.<sup>23,24</sup> To facilitate future



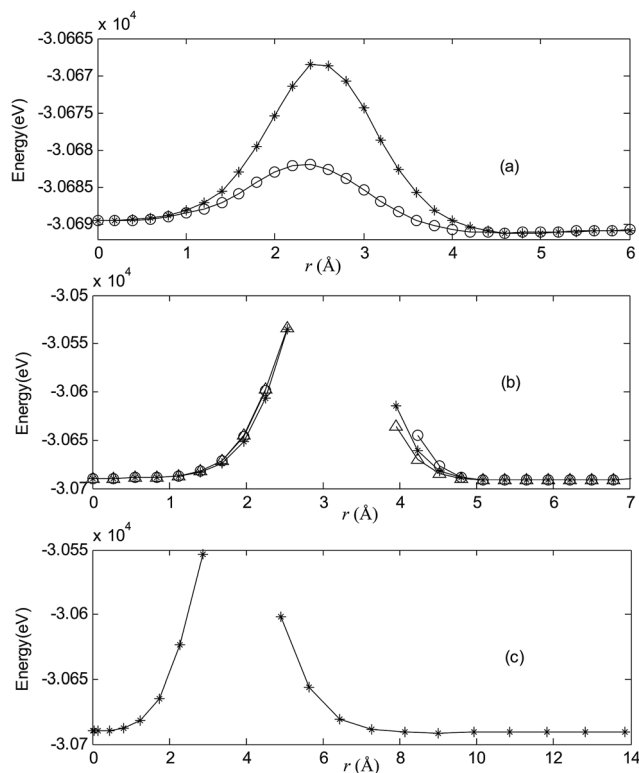


Fig. 6 Potential energy scan by moving the metal dopant Au from the cage center through different paths while keeping the cage intact for  $\text{AuB}_{40}^-$ .  $r$  represents the distance between the dopant Au and the cage center. (a) Asterisk represents the path  $L_z$ , circle represents the path  $L_y$ , (b) triangle represents the path  $L_{yz}$ , asterisk represents the path  $L_{xz}$ , circle represents the path  $L_{xyz}$ .

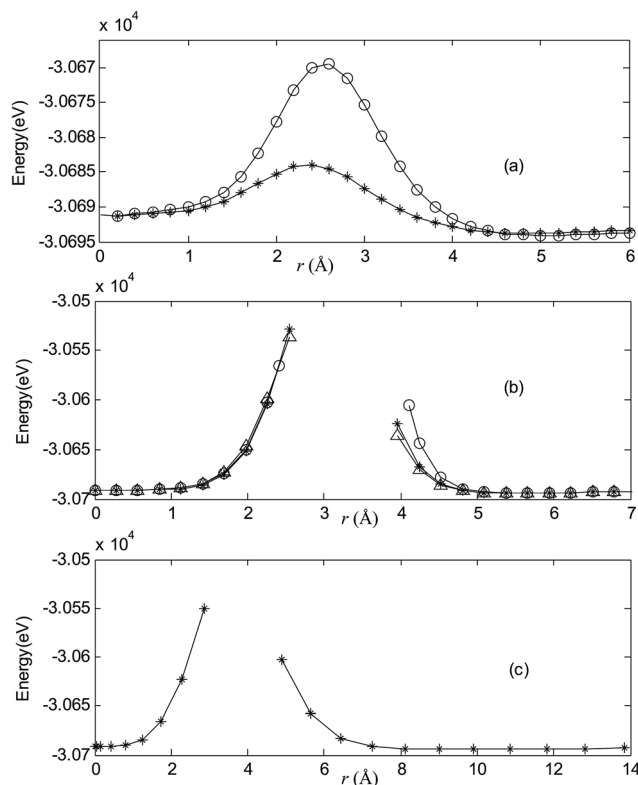


Fig. 7 Potential energy scan by moving the metal dopant Au from the cage center through different paths while keeping the cage intact for  $\text{AuB}_{40}^-$ .  $r$  represents the distance between the dopant Au and the cage center. (a) Asterisk represents the path  $L_z$ , circle represents the path  $L_y$ , (b) triangle represents the path  $L_{yz}$ , asterisk represents the path  $L_{xz}$ , circle represents the path  $L_{xyz}$ .

identifications of  $\text{MB}_{40}^-$  ( $M = \text{Cu, Ag, and Au}$ ), the adiabatic detachment energies (ADEs) for metalloborosphenes  $\text{MB}_{40}^-$  ( $M = \text{Cu, Ag, and Au}$ ) were calculated at the PBE0 level, then we calculated the vertical detachment energies (VDEs) and simulated the photoelectron spectra for metalloborosphenes  $\text{MB}_{40}^-$  ( $M = \text{Cu, Ag, and Au}$ ), using the time-dependent DFT (TD-DFT) method.<sup>23,24,64</sup> Adiabatic detachment energy of  $\text{MB}_{40}^-$  ( $M = \text{Cu, Ag, and Au}$ ) represents the electron affinity (EA) of corresponding neutral metalloborosphenes  $\text{MB}_{40}$  ( $M = \text{Cu, Ag, and Au}$ ). The larger EA can lead to the stronger probability of capturing an electron, *i.e.*, the neutral  $\text{MB}_{40}$  with larger EA is easier to capture an electron. Metalloborosphenes  $\text{MB}_{40}^-$  ( $M = \text{Cu, Ag, and Au}$ ) give the ground-state ADEs of 2.38( $\text{Cu@B}_{40}^-$ ), 2.53( $\text{Cu@B}_{40}^-$ ), 2.87( $\text{Ag@B}_{40}^-$ ), 2.53( $\text{Ag@B}_{40}^-$ ), 3.34( $\text{Au@B}_{40}^-$ ) and 2.94( $\text{Au@B}_{40}^-$ ) eV, respectively. Among the metalloborosphenes  $\text{MB}_{40}^-$  ( $M = \text{Cu, Ag, and Au}$ ),  $\text{Au@B}_{40}^-$  has the largest ADE (3.34 eV), which is larger than the ADE (2.29 eV)<sup>23</sup> of cage  $\text{B}_{40}^-$  and less than the ADE (3.51 eV)<sup>23</sup> of quasi-planar  $\text{B}_{40}^-$ . The calculated results indicate that ground-state ADEs of metalloborosphenes  $\text{MB}_{40}^-$  ( $M = \text{Cu, Ag, and Au}$ ) are larger than the ADE (2.29 eV)<sup>23</sup> of cage  $\text{B}_{40}^-$  and less than the ADE (3.51 eV)<sup>23</sup> of quasi-planar  $\text{B}_{40}^-$ , it suggests that doping of metal atom in  $\text{B}_{40}$  can increase the ADE.

Fig. 11 presents the photoelectron spectra (calculated VDEs were tabulated in Table S1†) of metalloborosphenes  $\text{MB}_{40}^-$  ( $M = \text{Cu, Ag, and Au}$ ). The predicted photoelectron spectra show

that  $\text{Cu@B}_{40}^-$  has the lowest first vertical detachment energy (VDE) and  $\text{Ag@B}_{40}^-$  has the largest energy gap (about 1.36 eV) between the first and second bands. The first several bands of photoelectron spectra were used to identify boron clusters,<sup>23,24</sup> so we will focus on the bands at the low binding energy side. The first peaks of these photoelectron spectra come from the calculated ground-state VDEs of  $\text{Cu@B}_{40}^-$ ,  $\text{Cu@B}_{40}^-$ ,  $\text{Ag@B}_{40}^-$ ,  $\text{Ag@B}_{40}^-$ ,  $\text{Au@B}_{40}^-$  and  $\text{Au@B}_{40}^-$  at 2.46, 2.64, 2.98, 2.63, 3.46 and 3.60 eV, respectively. The calculated ground-state VDEs of metalloborosphenes  $\text{MB}_{40}^-$  ( $M = \text{Cu, Ag, and Au}$ ) originate from the detachment of the electron from the molecular orbital (HOMO). The second peak of  $\text{Cu@B}_{40}^-$  comes from the second and third calculated VDEs at 3.22 and 3.25 eV which originate from detaching the electrons from HOMO-1 and HOMO-2. The second peaks of  $\text{Cu@B}_{40}^-$  come from the second and third calculated VDEs at 3.49 and 3.50 eV. The second peak of  $\text{Ag@B}_{40}^-$  comes from the second to fourth calculated VDEs at 4.34, 4.37, and 4.39 eV, respectively. The second to fourth calculated VDEs of metalloborospherene  $\text{Ag@B}_{40}^-$  originate from detaching the electrons from HOMO-1 to HOMO-3. The second peak of  $\text{Ag@B}_{40}^-$  comes from the second and third calculated VDEs, interestingly, the second and third calculated VDEs of metalloborospherene  $\text{Ag@B}_{40}^-$  are overlapped. The second peak of  $\text{Au@B}_{40}^-$  comes from the second to fourth calculated VDEs at 4.45, 4.52, and 4.54 eV, respectively. The



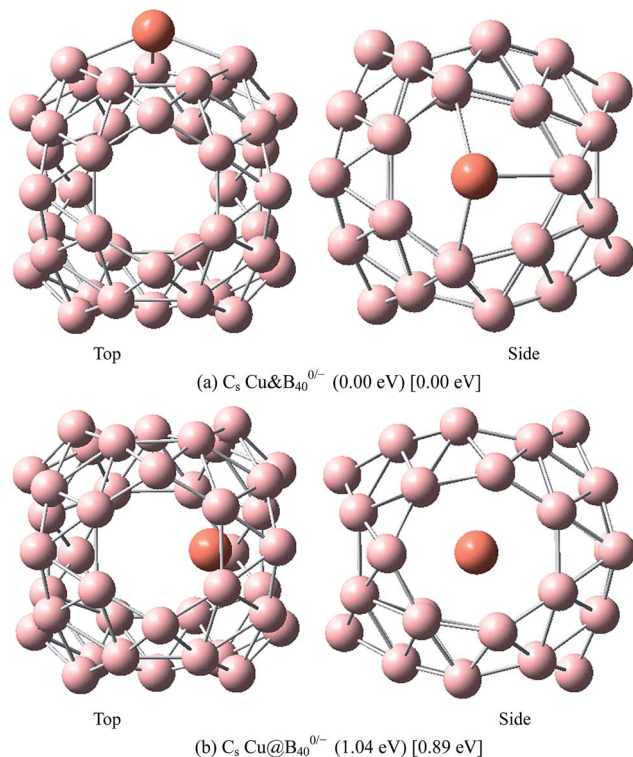


Fig. 8 The most stable endohedral and exohedral metalloborospherenes  $\text{CuB}_{40}^{0-}$ . The round brackets denote the relative energies of neutral metalloborospherenes  $\text{CuB}_{40}$  (the energy of exohedral  $\text{Cu}\&\text{B}_{40}$  is set to be zero) and the square brackets denote the relative energies of anionic metalloborospherenes  $\text{CuB}_{40}^{-}$  (the energy of exohedral  $\text{Cu}\&\text{B}_{40}^{-}$  is set to be zero).

second to fourth calculated VDEs of metalloborospherene  $\text{Au}\&\text{B}_{40}^{-}$  originate from detaching the electrons from HOMO–1 to HOMO–3. The second and third peaks of  $\text{Au}@B_{40}^{-}$  come from the second and third calculated VDEs at 4.17 and 4.38 eV, respectively. Fig. 11 indicates that metalloborospherenes  $\text{MB}_{40}^{-}$  ( $M = \text{Cu}, \text{Ag}, \text{and Au}$ ) have different spectral features, especially the endohedral and corresponding exohedral metalloborospherenes have different spectral bands at the low binding energy side. These features can be used to distinguish the metalloborospherenes  $\text{MB}_{40}^{-}$  ( $M = \text{Cu}, \text{Ag}, \text{and Au}$ ).

Fig. 11(a–f) and photoelectron spectra of borospherene  $\text{B}_{40}^{-}$  (see Fig. 11(g))<sup>23</sup> indicate that the addition of metal atom modifies the photoelectron spectra of borospherene  $\text{B}_{40}^{-}$  since the addition of extra atom modifies the electronic structure. The calculated results indicate that doping of metal atom in borospherene can increase the first VDE compared to the first VDE of  $\text{B}_{40}^{-}$ . The predicted photoelectron spectra in Fig. 11 provide important information for the identification of metalloborospherenes  $\text{MB}_{40}^{-}$  ( $M = \text{Cu}, \text{Ag}, \text{and Au}$ ). It is worth to note that the structures of atomic clusters cannot directly be identified by common analytical experimental methods, but they can indirectly be determined by using combined theoretical and experimental studies. As the discovery of  $\text{B}_{40}$ , if the photoelectron spectra of metalloborospherenes  $\text{MB}_{40}^{-}$  ( $M = \text{Cu}, \text{Ag}, \text{and Au}$ ) are obtained in experiments, these calculated characteristic

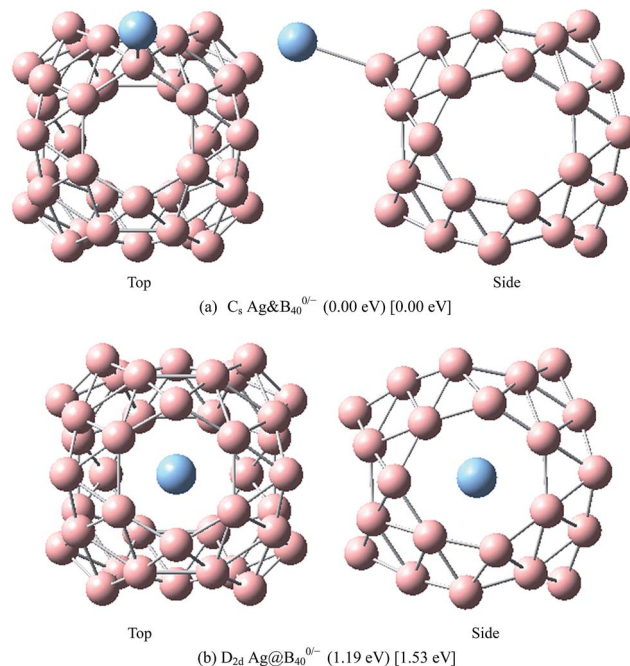


Fig. 9 The most stable endohedral and exohedral metalloborospherenes  $\text{AgB}_{40}^{0-}$ . The round brackets denote the relative energies of neutral metalloborospherenes  $\text{AgB}_{40}$  (the energy of exohedral  $\text{Ag}\&\text{B}_{40}$  is set to be zero) and the square brackets denote the relative energies of anionic metalloborospherenes  $\text{AgB}_{40}^{-}$  (the energy of exohedral  $\text{Ag}\&\text{B}_{40}^{-}$  is set to be zero).

bands may be used as theoretical basis for the identification of metalloborospherenes  $\text{MB}_{40}^{-}$  ( $M = \text{Cu}, \text{Ag}, \text{and Au}$ ).

### Infrared spectra

Infrared spectra of metalloborospherenes  $\text{MB}_{40}^{0-}$  ( $M = \text{Cu}, \text{Ag}, \text{and Au}$ ) are given in Fig. 12 (spectral data were tabulated in Tables S2–S13<sup>†</sup>), these infrared peaks distribute in three regions: low frequency region (from  $0 \text{ cm}^{-1}$  to  $500 \text{ cm}^{-1}$ ), middle frequency region (from  $500 \text{ cm}^{-1}$  to  $1000 \text{ cm}^{-1}$ ) and high frequency region (from  $1000 \text{ cm}^{-1}$  to  $1400 \text{ cm}^{-1}$ ), and the main strong infrared peaks are located in the high frequency region (from  $1000 \text{ cm}^{-1}$  to  $1400 \text{ cm}^{-1}$ ). The highest frequency is  $1323 \text{ cm}^{-1}$  for  $\text{Cu}\&\text{B}_{40}$ ,  $1319 \text{ cm}^{-1}$  for  $\text{Cu}\&\text{B}_{40}^{-}$ ,  $1314 \text{ cm}^{-1}$  for  $\text{Cu}@B_{40}$ ,  $1305 \text{ cm}^{-1}$  for  $\text{Cu}@B_{40}^{-}$ ,  $1320 \text{ cm}^{-1}$  for  $\text{Ag}\&\text{B}_{40}$ ,  $1314 \text{ cm}^{-1}$  for  $\text{Ag}\&\text{B}_{40}^{-}$ ,  $1307 \text{ cm}^{-1}$  for  $\text{Ag}@B_{40}$ ,  $1299 \text{ cm}^{-1}$  for  $\text{Ag}@B_{40}^{-}$ ,  $1320 \text{ cm}^{-1}$  for  $\text{Au}\&\text{B}_{40}$ ,  $1316 \text{ cm}^{-1}$  for  $\text{Au}\&\text{B}_{40}^{-}$ ,  $1304 \text{ cm}^{-1}$  for  $\text{Au}@B_{40}$ , and  $1306 \text{ cm}^{-1}$  for  $\text{Au}@B_{40}^{-}$ . These vibrational modes are formed by stretching vibrations of boron atoms. In addition, they are close to the highest vibrational frequency of  $D_{2d} \text{B}_{40}$  ( $1327 \text{ cm}^{-1}$ ). The lowest vibrational frequency is  $116 \text{ cm}^{-1}$  for  $\text{Cu}\&\text{B}_{40}$ ,  $107 \text{ cm}^{-1}$  for  $\text{Cu}\&\text{B}_{40}^{-}$ ,  $89 \text{ cm}^{-1}$  for  $\text{Cu}@B_{40}$ ,  $92 \text{ cm}^{-1}$  for  $\text{Cu}@B_{40}^{-}$ ,  $25 \text{ cm}^{-1}$  for  $\text{Ag}\&\text{B}_{40}$ ,  $36 \text{ cm}^{-1}$  for  $\text{Ag}\&\text{B}_{40}^{-}$ ,  $47 \text{ cm}^{-1}$  for  $\text{Ag}@B_{40}$ ,  $52 \text{ cm}^{-1}$  for  $\text{Ag}@B_{40}^{-}$ ,  $34 \text{ cm}^{-1}$  for  $\text{Au}\&\text{B}_{40}$ ,  $44 \text{ cm}^{-1}$  for  $\text{Au}\&\text{B}_{40}^{-}$ ,  $25 \text{ cm}^{-1}$  for  $\text{Au}@B_{40}$ , and  $67 \text{ cm}^{-1}$  for  $\text{Au}@B_{40}^{-}$ . These vibrational modes are formed by vibrations of metal atoms. Unlike the highest frequencies of metalloborospherenes  $\text{MB}_{40}^{0-}$  ( $M = \text{Cu}, \text{Ag}, \text{and Au}$ ), these lowest vibrational frequencies of



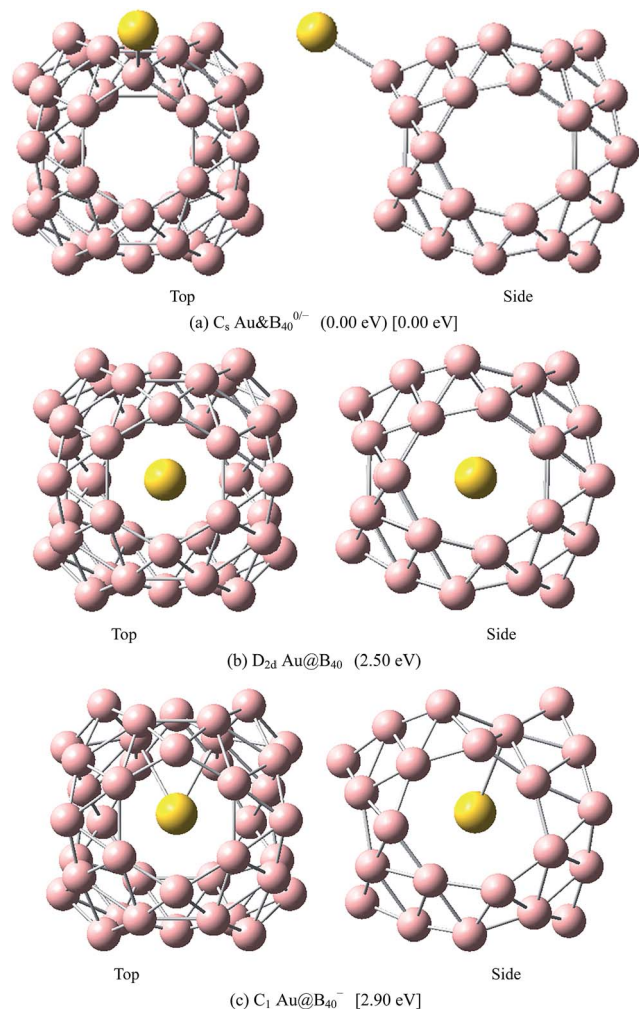


Fig. 10 The most stable endohedral and exohedral metalloborospherenes  $AuB_{40}^{0-}$ . The round brackets denote the relative energies of neutral metalloborospherenes  $AuB_{40}$  (the energy of exohedral  $Au&B_{40}$  is set to be zero) and the square brackets denote the relative energies of anionic metalloborospherenes  $AuB_{40}^{0-}$  (the energy of exohedral  $Au&B_{40}^-$  is set to be zero).

metalloborospherenes  $MB_{40}^{0-}$  ( $M = Cu, Ag, \text{ and } Au$ ) are much lower than the lowest vibrational frequency of borospherene  $B_{40}$  ( $170 \text{ cm}^{-1}$ ).

The sharpest peaks of  $Cu&B_{40}$ ,  $Cu&B_{40}^-$ ,  $Cu@B_{40}$ ,  $Cu@B_{40}^-$ ,  $Ag&B_{40}$ ,  $Ag&B_{40}^-$ ,  $Ag@B_{40}$ ,  $Ag@B_{40}^-$ ,  $Au&B_{40}$ ,  $Au&B_{40}^-$ ,  $Au@B_{40}$  and  $Au@B_{40}^-$  are at 1275, 1265, 1265, 1266, 1270, 1262, 1278, 1271, 1271, 1268, 1247 and  $1217 \text{ cm}^{-1}$ , respectively. These vibrational modes are formed by stretching vibrations of boron atoms. Note that the most sharpest peaks of metalloborospherenes  $MB_{40}^{0-}$  ( $M = Cu, Ag, \text{ and } Au$ ) are located at about  $1270 \text{ cm}^{-1}$  and almost same with the location (at  $1274 \text{ cm}^{-1}$ ) of sharpest peak for borospherene  $B_{40}$ .<sup>40</sup> Owing to the high symmetry ( $D_{2d}$ ) of  $Ag@B_{40}$ ,  $Ag@B_{40}^-$ , and  $Au@B_{40}$ , there are doubly degenerate vibrational modes. However, the other structures have only non-degenerate vibrational modes. Like the infrared spectra of borospherene  $B_{40}$ ,<sup>39,40</sup> some vibrational modes of endohedral  $Ag@B_{40}^{0-}$  and  $Au@B_{40}$  are infrared

inactive. However, all the vibrational modes of other structures are infrared active modes, it suggest that doping of metal atom can add the spectra active modes.

It's worth noting that Fig. 12(e and i) show that exohedral  $Ag&B_{40}$  and  $Au&B_{40}$  have similar infrared spectra, and Fig. 12(f and j) show that exohedral  $Ag&B_{40}^-$  and  $Au&B_{40}^-$  have similar infrared spectra. In addition, Fig. 12(g and h) show that endohedral  $Ag@B_{40}$  and  $Ag@B_{40}^-$  have similar infrared spectra, but the main peaks of anionic  $Ag@B_{40}^-$  are redshifted somewhat since the extra electron modifies the electronic structures. It's worth noting that the infrared spectra of endohedral  $Ag@B_{40}^{0-}$  are quite similar to that of dianion  $B_{40}^{2-}$  (see Fig. 12(n)).<sup>40</sup> However, Fig. 12(k) shows that the infrared spectra of endohedral  $Au@B_{40}$  is similar to that of  $B_{40}$  (see Fig. 12(m)). Except for  $Ag@B_{40}^{0-}$  and  $Au@B_{40}$ , infrared spectra of other metalloborospherenes are different from that of  $B_{40}^{0-}$ ,<sup>40</sup> the metal dopant in  $B_{40}$  changes the IR spectra of  $B_{40}$  such as some weakened vibrational modes and some enhanced characteristic peaks. These spectral characteristics suggest that location of dopant and charge of metalloborospherene play an important role in infrared spectra. The predicted infrared spectra also provide some information for the identification of metalloborospherenes  $MB_{40}^{0-}$  ( $M = Cu, Ag, \text{ and } Au$ ), these different characteristic peaks also provide a theoretical basis for the identification and confirmation of metalloborospherenes  $MB_{40}^{0-}$  ( $M = Cu, Ag, \text{ and } Au$ ).

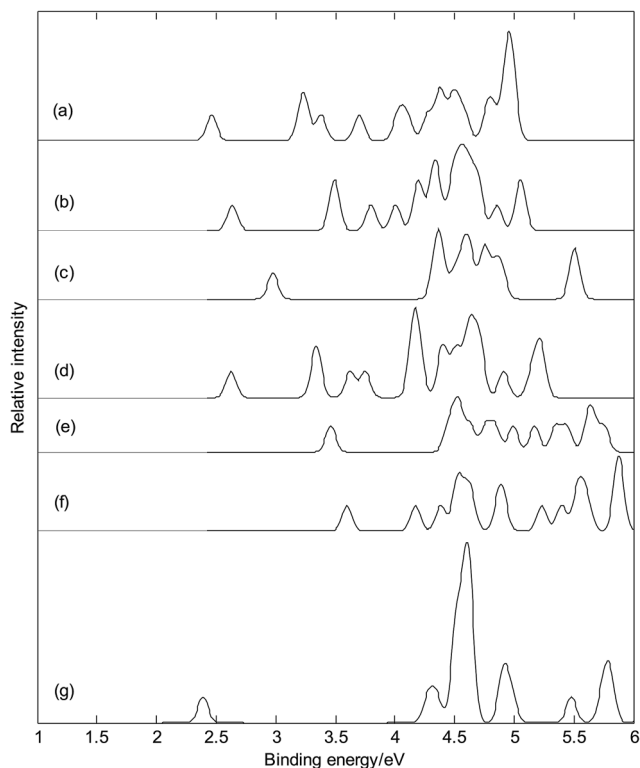
### Raman spectra

Fig. 13 depicts the Raman spectra of metalloborospherenes  $MB_{40}^{0-}$  ( $M = Cu, Ag, \text{ and } Au$ ), the sharpest peaks of  $Cu&B_{40}$ ,  $Cu&B_{40}^-$ ,  $Cu@B_{40}$ ,  $Cu@B_{40}^-$ ,  $Ag&B_{40}$ ,  $Ag&B_{40}^-$ ,  $Ag@B_{40}$ ,  $Ag@B_{40}^-$ ,  $Au&B_{40}$ ,  $Au&B_{40}^-$ ,  $Au@B_{40}$  and  $Au@B_{40}^-$  are at 435, 1265, 1238, 654, 685, 672, 1229, 775, 1320, 737, 1304 and  $1306 \text{ cm}^{-1}$ , respectively. Unlike the infrared spectra of  $MB_{40}^{0-}$  ( $M = Cu, Ag, \text{ and } Au$ ), the sharpest Raman peaks of metalloborospherenes  $MB_{44}^{0-}$  ( $M = Li, Na, \text{ and } K$ ) are at middle or high frequency region. Among the Raman active modes, the typical radial breathing modes of  $Cu&B_{40}$ ,  $Cu&B_{40}^-$ ,  $Cu@B_{40}$ ,  $Cu@B_{40}^-$ ,  $Ag&B_{40}$ ,  $Ag&B_{40}^-$ ,  $Ag@B_{40}$ ,  $Ag@B_{40}^-$ ,  $Au&B_{40}$ ,  $Au&B_{40}^-$  and  $Au@B_{40}$  are at 166, 145, 166, 181, 175, 171, 153, 158, 175, 173 and  $157 \text{ cm}^{-1}$ , respectively, which are similar to the typical radial breathing mode of  $B_{40}$  at  $170 \text{ cm}^{-1}$ .<sup>66</sup> The breathing modes are used to identify the hollow structures in nanotubes. These typical radial breathing modes are close to the location of  $B_{40}$ , it suggests that the addition of metal atoms just lead to small change of  $B_{40}$  configuration. However,  $Au@B_{40}^-$  has not the radial breathing mode near the frequency of  $170 \text{ cm}^{-1}$  which further indicates that  $Au@B_{40}^-$  has obvious changes. The calculated results indicate that all the vibrational modes of exohedral  $MB_{40}^{0-}$  ( $M = Cu, Ag, \text{ and } Au$ ) and endohedral  $Cu@B_{40}^{0-}$  and  $Au@B_{40}^-$  are infrared active and Raman active. However, like the borospherene  $B_{40}$ ,<sup>39,40</sup> there are some silent modes in endohedral  $Ag@B_{40}^{0-}$  and  $Au@B_{40}$ , which means that these vibrational modes are Raman inactive and infrared inactive.



**Table 1** The symmetries, relative energies (neutral  $\text{CuB}_{40}$ : the energy of  $\text{Cu}\text{B}_{40}$  is set to be zero, anionic  $\text{CuB}_{40}^-$ : the energy of  $\text{Cu}\text{B}_{40}^-$  is set to be zero, neutral  $\text{AgB}_{40}$ : the energy of  $\text{Ag}\text{B}_{40}$  is set to be zero, anionic  $\text{AgB}_{40}^-$ : the energy of  $\text{Ag}\text{B}_{40}^-$  is set to be zero, neutral  $\text{AuB}_{40}$ : the energy of  $\text{Au}\text{B}_{40}$  is set to be zero, anionic  $\text{AuB}_{40}^-$ : the energy of  $\text{Au}\text{B}_{40}^-$  is set to be zero), energy gaps ( $E_g$ ), dipole moments ( $\mu$ ), lowest frequencies, and states of metalloborospherenes  $\text{MB}_{40}^{0/-}$  ( $M = \text{Cu}, \text{Ag}, \text{and Au}$ ). The superscripts a and b denote the alpha electron and beta electron, respectively

	Symmetry	Relative energy/eV	$E_g$ /eV	$\mu$ /Debye	State	Lowest frequency/ $\text{cm}^{-1}$
$\text{Cu}\text{B}_{40}$	$C_s$	0.00	1.40 <sup>a</sup> 3.00 <sup>b</sup>	0.82	$^2A'$	116
$\text{Cu}\text{B}_{40}^-$	$C_s$	0.00	1.21	0.68	$^1A'$	107
$\text{Cu}@B_{40}$	$C_s$	1.04	1.53 <sup>a</sup> 2.88 <sup>b</sup>	0.39	$^2A'$	89
$\text{Cu}@B_{40}^-$	$C_s$	0.89	1.52	0.56	$^1A'$	92
$\text{Ag}\text{B}_{40}$	$C_s$	0.00	2.12 <sup>a</sup> 2.52 <sup>b</sup>	3.78	$^2A'$	25
$\text{Ag}\text{B}_{40}^-$	$C_s$	0.00	1.83	3.49	$^1A'$	36
$\text{Ag}@B_{40}$	$D_{2d}$	1.19	1.44 <sup>a</sup> 2.99 <sup>b</sup>	0.00	$^2B_2$	47
$\text{Ag}@B_{40}^-$	$D_{2d}$	1.53	1.51	0.00	$^1A_1$	52
$\text{Au}\text{B}_{40}$	$C_s$	0.00	2.45 <sup>a</sup> 2.21 <sup>b</sup>	0.65	$^2A'$	34
$\text{Au}\text{B}_{40}^-$	$C_s$	0.00	2.20	4.76	$^1A'$	44
$\text{Au}@B_{40}$	$D_{2d}$	2.50	1.80 <sup>a</sup> 3.14 <sup>b</sup>	0.00	$^2A_1$	25
$\text{Au}@B_{40}^-$	$C_1$	2.90	2.30	2.46	$^1A$	67



**Fig. 11** Simulated photoelectron spectra of metalloborospherenes  $\text{MB}_{40}^-$  ( $M = \text{Cu}, \text{Ag}, \text{and Au}$ ) and borospherene  $\text{B}_{40}^-$ . (a):  $C_s$   $\text{Cu}\text{B}_{40}^-$ , (b):  $C_s$   $\text{Cu}@B_{40}^-$ , (c):  $C_s$   $\text{Ag}\text{B}_{40}^-$ , (d):  $D_{2d}$   $\text{Ag}@B_{40}^-$ , (e):  $C_s$   $\text{Au}\text{B}_{40}^-$ , (f):  $C_1$   $\text{Au}@B_{40}^-$ , (g):  $D_{2d}$   $\text{B}_{40}^-$ . The simulations were done by fitting the distributions of calculated vertical detachment energies at the PBE0 level with unit-area Gaussian functions of 0.05 eV half-width.

Fig. 13(g and h) show that endohedral  $\text{Ag}@B_{40}$  and  $\text{Ag}@B_{40}^-$  have the similar Raman spectra, however, the addition of an electron weakens the main characteristic peaks. It's worth noting that the Raman spectra of endohedral  $\text{Ag}@B_{40}^{0/-}$  are some

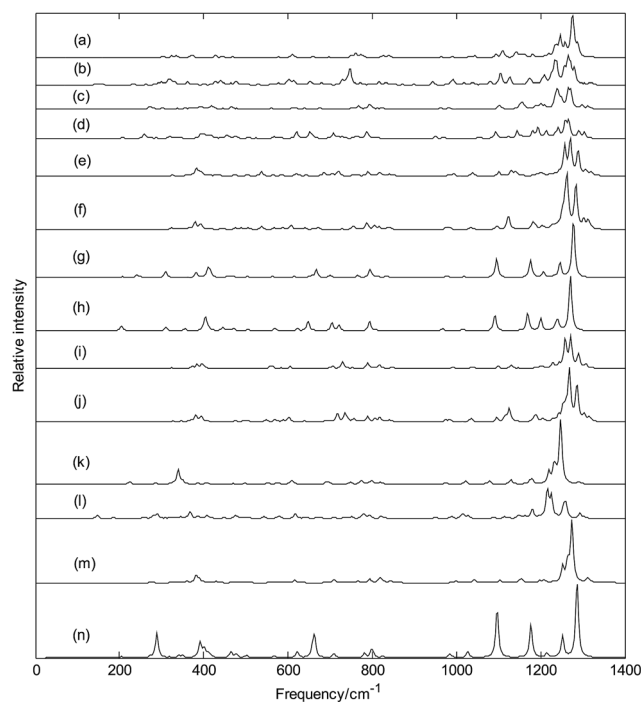


**Fig. 12** Predicted infrared spectra of metalloborospherenes  $\text{MB}_{40}^{0/-}$  ( $M = \text{Cu}, \text{Ag}, \text{and Au}$ ) and borospherenes  $\text{B}_{40}^{0/-}$ . (a):  $C_s$   $\text{Cu}\text{B}_{40}$ , (b):  $C_s$   $\text{Cu}\text{B}_{40}^-$ , (c):  $C_s$   $\text{Cu}@B_{40}$ , (d):  $C_s$   $\text{Cu}@B_{40}^-$ , (e):  $C_s$   $\text{Ag}\text{B}_{40}$ , (f):  $C_s$   $\text{Ag}\text{B}_{40}^-$ , (g):  $D_{2d}$   $\text{Ag}@B_{40}$ , (h):  $D_{2d}$   $\text{Ag}@B_{40}^-$ , (i):  $C_s$   $\text{Au}\text{B}_{40}$ , (j):  $C_s$   $\text{Au}\text{B}_{40}^-$ , (k):  $D_{2d}$   $\text{Au}@B_{40}$ , (l):  $C_1$   $\text{Au}@B_{40}^-$ , (m):  $D_{2d}$   $\text{B}_{40}$ , (n):  $D_{2d}$   $\text{B}_{40}^-$ .



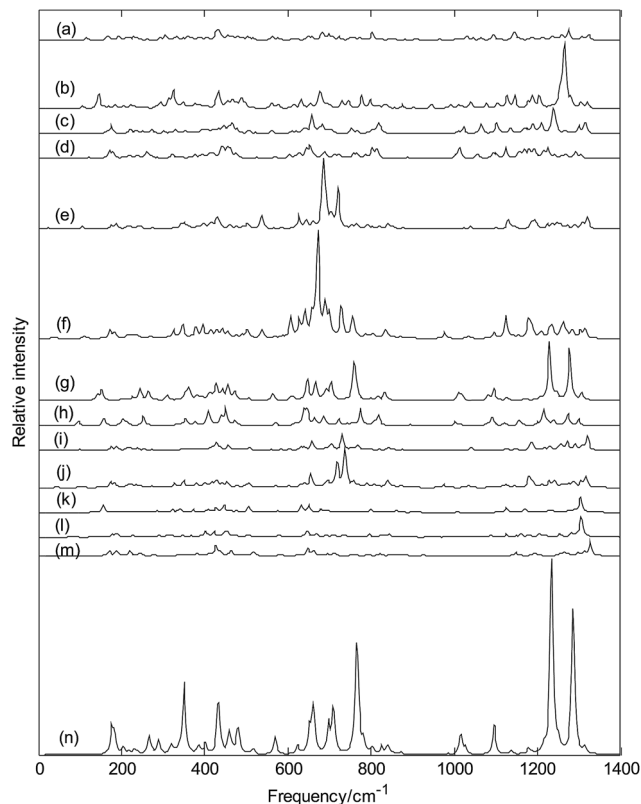


Fig. 13 Predicted Raman spectra of metalloborospherenes  $MB_{40}^{0/-}$  ( $M = \text{Cu, Ag, and Au}$ ) and borospherenes  $B_{40}^{0/-}$ . (a):  $C_s \text{Cu}\delta B_{40}$ , (b):  $C_s \text{Cu}\delta B_{40}^-$ , (c):  $C_s \text{Cu}\textcircled{B}_{40}$ , (d):  $C_s \text{Cu}\textcircled{B}_{40}^-$ , (e):  $C_s \text{Ag}\delta B_{40}$ , (f):  $C_s \text{Ag}\delta B_{40}^-$ , (g):  $D_{2d} \text{Ag}\textcircled{B}_{40}$ , (h):  $D_{2d} \text{Ag}\textcircled{B}_{40}^-$ , (i):  $C_s \text{Au}\delta B_{40}$ , (j):  $C_s \text{Au}\delta B_{40}^-$ , (k):  $D_{2d} \text{Au}\textcircled{B}_{40}$ , (l):  $C_1 \text{Au}\textcircled{B}_{40}^-$ , (m):  $D_{2d} B_{40}$ , (n):  $D_{2d} B_{40}^-$ .

similar to that of dianion  $B_{40}^{2-}$  (see Fig. 13(n)) and Raman spectra of endohedral  $\text{Au}\textcircled{B}_{40}$  are some similar to that of  $B_{40}$  (see Fig. 13(m)).<sup>34</sup> Except for  $\text{Ag}\textcircled{B}_{40}^{0/-}$  and  $\text{Au}\textcircled{B}_{40}$ , Fig. 13 indicates that doping of metal atom in  $B_{40}$  also changes the Raman peaks of  $B_{40}$  such as some weakened vibrational modes and some enhanced characteristic peaks.<sup>40</sup> In addition, Raman spectra of endohedral metalloborospherenes are different from that of corresponding exohedral metalloborospherenes, these spectral characteristics can be used to identify the endohedral and exohedral configurations.

Raman spectra, as the supplement of infrared spectra, can be used for the basis of identification of metalloborospherenes  $MB_{40}^{0/-}$  ( $M = \text{Cu, Ag, and Au}$ ). From the infrared and Raman spectra of each metalloborospherene, we can find, at some frequencies, infrared absorption peaks are strong, but the Raman peaks are very weak. However, at some frequencies, infrared absorption peaks are very weak (or infrared inactive), but the Raman peaks are strong. In addition, at some frequencies, both the infrared and Raman peaks are strong. Infrared intensity is proportional to  $|\partial\bar{\mu}/\partial Q_i|^2$ ,<sup>67,68</sup> where  $\bar{\mu}$  is the electric dipole moment and  $Q_i$  is the normal-mode coordinate. A vibrational mode of molecular with no change of dipole moment is infrared inactive, we can't obtain the normal mode frequency from the infrared spectral data in experiments.

However, this vibrational mode may lead to the change of polarizability, this indicates that the vibrational mode is Raman active. The calculated Raman spectra can be useful for analytical purposes and contribute significantly to spectral interpretation and vibrational assignments, also can provide technical guidance for future synthesis.

### Electronic absorption spectra

Finally, we calculated electronic absorption spectra of exohedral metalloborospherenes  $M\&B_{40}^{0/-}$  ( $M = \text{Cu, Ag, and Au}$ ), as shown in Fig. 14. The previous research results show that  $B_{40}$  has only UV-Vis absorption bands (see Fig. 14(g)),<sup>39,40</sup> however, one can observe several near infrared (NIR) absorption bands of metalloborospherenes  $M\&B_{40}^{0/-}$  ( $M = \text{Cu, Ag, and Au}$ ) from 780 to 3000 nm. It suggests that doping of metal atom in  $B_{40}$  can redshift the electronic spectra. Fig. 14(a) presents the electronic spectra of  $\text{Cu}\&B_{40}$ , the largest excitation wavelength (first excited state) is 2175 nm. The absorption band in region NIR from 1500 to 2500 nm comes from the first three excited states which originate from the electron transitions from  $\alpha$ -HOMO to  $\alpha$ -LUMO/ $\alpha$ -LUMO+1/ $\alpha$ -LUMO+2. Fig. 14(b) presents the electronic absorption spectra of  $\text{Cu}\&B_{40}^-$ , the largest excitation wavelength is 2701 nm. The absorption band in region NIR from 2500 to 3000 nm comes from the first excited state which

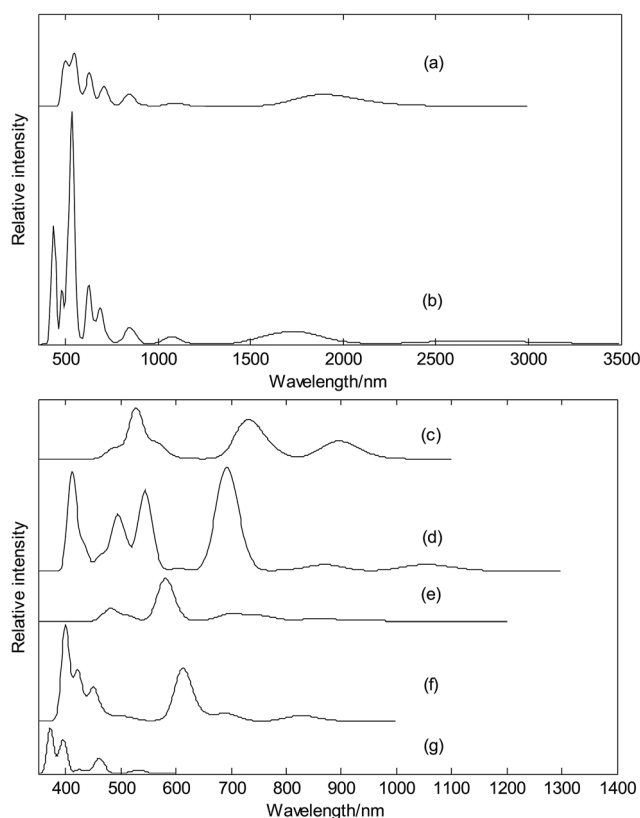


Fig. 14 Predicted electronic absorption spectra of exohedral metalloborospherenes  $MB_{40}^{0/-}$  ( $M = \text{Cu, Ag, and Au}$ ) and borospherene  $B_{40}$ . (a):  $C_s \text{Cu}\delta B_{40}$ , (b):  $C_s \text{Cu}\delta B_{40}^-$ , (c):  $C_s \text{Ag}\delta B_{40}$ , (d):  $C_s \text{Ag}\delta B_{40}^-$ , (e):  $C_s \text{Au}\delta B_{40}$ , (f):  $C_s \text{Au}\delta B_{40}^-$ , (g):  $D_{2d} B_{40}$ .



originates from the electron transitions from HOMO to LUMO. Fig. 14(a and b) indicate that electronic spectra of  $\text{Cu@B}_{40}^-$  are apparently red-shifted comparing with  $\text{Cu@B}_{40}$ . Fig. 14(c) presents the electronic spectra of the  $\text{Ag@B}_{40}$ . The largest excitation wavelength is 898 nm. The absorption band in region NIR from 800 to 1000 nm comes from the first two excited states which originate from the electron transitions of  $\alpha\text{-HOMO} \rightarrow \alpha\text{-LUMO}/\alpha\text{-LUMO}+1$  coupled with  $\beta\text{-HOMO}/\beta\text{-HOMO}-1/\beta\text{-HOMO}-2/\beta\text{-HOMO}-7 \rightarrow \beta\text{-LUMO}$ . Fig. 14(d) presents the electronic spectra of the  $\text{Ag@B}_{40}^-$ . The largest excitation wavelength is 1054 nm. The absorption band in region NIR from 1000 to 1200 nm comes from the first excited state which originates from the electron transitions from HOMO to LUMO/LUMO+2. Fig. 14(e) presents the electronic absorption spectra of the  $\text{Au@B}_{40}$ , the largest excitation wavelength is 988 nm. The weak absorption band in region NIR from 800 to 1000 nm comes from the first four excited states which originate from the electron transitions of  $\alpha\text{-HOMO} \rightarrow \alpha\text{-LUMO}+1$  coupled with  $\beta\text{-HOMO}/\beta\text{-HOMO}-1/\beta\text{-HOMO}-2/\beta\text{-HOMO}-3/\beta\text{-HOMO}-4 \rightarrow \beta\text{-LUMO}$ . Fig. 14(f) presents the electronic absorption spectra of the  $\text{Au@B}_{40}^-$ , the largest excitation wavelength is 828 nm. The absorption band in region NIR from 780 to 900 nm comes from the first excited state which originates from the electron transitions from HOMO to LUMO. Other NIR absorption bands of metalloborospherenes  $\text{MB}_{40}^{0/-}$  (M = Cu, Ag, and Au) come from the higher excited states which originate from the electron transitions of corresponding orbitals.

For the metalloborospherenes  $\text{M@B}_{40}^-$  (M = Cu, Ag, and Au) with closed-shell electronic structure, the minimum excitation energy (the largest excitation wavelength) mainly comes from the electron transition from HOMO to LUMO. HOMO–LUMO energy gap reflects the probability of the molecules jumping from ground state to excited state. Generally speaking, the larger energy gap can lead to the larger electron excitation energy, *i.e.*, the smaller the probability of electronic transition. On the contrary, the molecule with smaller energy gap is easier to jump to the excited state. According to the previous results, the HOMO–LUMO energy gaps are 1.2113, 1.8272 and 2.1975 eV for  $\text{Cu@B}_{40}^-$ ,  $\text{Ag@B}_{40}^-$ , and  $\text{Au@B}_{40}^-$ , respectively. Although the energy gap of ground state does not represent the minimum excitation energy, the increasing HOMO–LUMO energy gaps just reflect the decreasing largest excitation wavelengths 2701, 1054 and 828 nm for  $\text{Cu@B}_{40}^-$ ,  $\text{Ag@B}_{40}^-$ , and  $\text{Au@B}_{40}^-$ , respectively. The calculated electronic spectra may be used for the structural analysis in conjunction with other techniques.

## Conclusions

In a summary, the structures, stabilities, photoelectron spectra, infrared spectra, Raman spectra, and electronic absorption spectra of metalloborospherenes  $\text{MB}_{40}^-$  (M = Cu, Ag, and Au) have been studied at the level of density functional theory (DFT) and time-dependent density functional theory (TD-DFT). Potential energy scan confirms that there are two possible ground state geometries where dopant can exist outside or inside cage. In addition, potential energy scan

confirms metalloborospherenes  $\text{MB}_{40}^-$  (M = Ag and Au) have a very high energy barrier around the surface of  $\text{B}_{40}$  and the energy barrier can confine dopant inside  $\text{B}_{40}$ . The further calculated results suggest that Cu, Ag, and Au atoms can form stable exohedral metalloborospherenes  $\text{M@B}_{40}^{0/-}$  (M = Cu, Ag, and Au) and endohedral metalloborospherenes  $\text{M@B}_{40}^{0/-}$  (M = Cu, Ag, and Au). In addition, relative energies of these metalloborospherenes reveal that the Cu, Ag, and Au atoms favor the exohedral configuration. The calculated photoelectron spectra show that metalloborospherenes  $\text{MB}_{40}^-$  (M = Cu, Ag, and Au) have different and meaningful photoelectron spectra which can be used as theoretical basis for the identification of metalloborospherenes  $\text{MB}_{40}^-$  (M = Cu, Ag, and Au). The calculated infrared spectra suggest that location of dopant and charge of metalloborospherenes play an important role in infrared spectra. In addition, the calculated electronic spectra indicate that metalloborospherenes  $\text{MB}_{40}^-$  (M = Cu, Ag, and Au) have obvious near-IR absorption peaks. These spectral features are readily compared with future spectroscopy measurements and can be used as fingerprints to identify and distinguish the metalloborospherenes  $\text{MB}_{40}^-$  (M = Cu, Ag, and Au). The metalloborospherenes  $\text{MB}_{40}^{0/-}$  (M = Cu, Ag, and Au) have provided an important clue for the development of new boron-based materials such as molecular device.

## Conflict of interest

There are no conflicts of interest to declare.

## Acknowledgements

This work was supported by the Growth Foundation for Young Scientists of Education Department of Guizhou Province, China (Grant No. QJH KY[2016]217), and the International Science & Technology Cooperation Program of China (Grant No. 2014DFA00670).

## Notes and references

- 1 H. W. Kroto, J. R. Heath, S. C. O'Brien, R. F. Curl and R. E. Smalley, *Nature*, 1985, **318**, 162.
- 2 H. J. Zhai, B. Kiran, J. Li and L. S. Wang, *Nat. Mater.*, 2003, **2**, 827.
- 3 I. A. Popov, Z. A. Piazza, W. L. Li, L. S. Wang and A. I. Boldyrev, *J. Chem. Phys.*, 2013, **139**, 144307.
- 4 Z. A. Piazza, H. S. Hu, W. L. Li, Y. F. Zhao, J. Li and L. S. Wang, *Nat. Commun.*, 2014, **5**, 3113.
- 5 A. P. Sergeeva, D. Y. Zubarev, H. J. Zhai, A. I. Boldyrev and L. S. Wang, *J. Am. Chem. Soc.*, 2008, **130**, 7244.
- 6 W. L. Li, Q. Chen, W. J. Tian, H. Bai, Y. F. Zhao, H. S. Hu, J. Li, H. J. Zhai, S. D. Li and L. S. Wang, *J. Am. Chem. Soc.*, 2014, **136**, 12257.
- 7 E. Oger, N. R. Crawford, R. Kelting, P. Weis, M. M. Kappes and R. Ahlrichs, *Angew. Chem., Int. Ed.*, 2007, **46**, 8503.
- 8 A. N. Alexandrova, A. I. Boldyrev, H. J. Zhai and L. S. Wang, *Coord. Chem. Rev.*, 2006, **250**, 2811.



- 9 A. P. Sergeeva, I. A. Popov, Z. A. Piazza, W. L. Li, C. Romanescu, L. S. Wang and A. I. Boldyrev, *Acc. Chem. Res.*, 2014, **47**, 1349.
- 10 N. G. Szwacki, A. Sadrzadeh and B. I. Yakobson, *Phys. Rev. Lett.*, 2007, **98**, 166804.
- 11 X. L. Sheng, Q. B. Yan, Q. R. Zheng and G. Su, *Phys. Chem. Chem. Phys.*, 2009, **11**, 9696.
- 12 L. Wang, J. J. Zhao, F. Y. Li and Z. F. Chen, *Chem. Phys. Lett.*, 2010, **501**, 16.
- 13 C. Özdoğan, S. Mukhopadhyay, W. Hayami, Z. B. Güvenç, R. Pandey and I. Boustani, *J. Phys. Chem. C*, 2010, **114**, 4362.
- 14 L. J. Cheng, *J. Chem. Phys.*, 2012, **136**, 104301.
- 15 H.-G. Lu and S. D. Li, *J. Chem. Phys.*, 2013, **139**, 224307.
- 16 J. Lv, Y. C. Wang, L. Zhu and Y. M. Ma, *Nanoscale*, 2014, **6**, 11692–11696.
- 17 H. T. Pham, L. V. Duong and M. T. Nguyen, *J. Phys. Chem. C*, 2014, **118**, 24181.
- 18 L. V. Duong, H. T. Pham, N. M. Tam and M. T. Nguyen, *Phys. Chem. Chem. Phys.*, 2014, **16**, 19470.
- 19 T. B. Tai, L. V. Duong, H. T. Pham, D. T. T. Maia and M. T. Nguyen, *Chem. Commun.*, 2014, **50**, 1558.
- 20 H. Tang and S. Ismail-Beigi, *Phys. Rev. Lett.*, 2007, **99**, 115501.
- 21 D. L. V. K. Prasad and E. D. Jemmis, *Phys. Rev. Lett.*, 2008, **100**, 165504.
- 22 D. L. V. K. Prasad and E. D. Jemmis, *Appl. Phys. Lett.*, 2010, **96**, 023108.
- 23 H. J. Zhai, Y. F. Zhao, W. L. Li, Q. Chen, H. Bai, H. S. Hu, Z. A. Piazza, W. J. Tian, H. G. Lu, Y. B. Wu, Y. W. Mu, G. F. Wei, Z. P. Liu, J. Li, S. D. Li and L. S. Wang, *Nat. Chem.*, 2014, **6**, 727.
- 24 Q. Chen, W. L. Li, Y. F. Zhao, S. Y. Zhang, H. S. Hu, H. Bai, H. R. Li, W. J. Tian, H. G. Lu, H. J. Zhai, S. D. Li, J. Li and L. S. Wang, *ACS Nano*, 2015, **9**, 754.
- 25 G. Martínez-Guajardo, J. L. Cabellos, A. Díaz-Celaya, S. Pan, R. Islas, P. K. Chattaraj, T. Heine and G. Merino, *Sci. Rep.*, 2015, **5**, 11287.
- 26 H. L. Dong, T. J. Hou, S. T. Lee and Y. Y. Li, *Sci. Rep.*, 2015, **5**, 09952.
- 27 I. A. Popov, T. Jian, G. V. Lopez, A. I. Boldyrev and L. S. Wang, *Nat. Commun.*, 2015, **6**, 8654.
- 28 T. Jian, W. L. Li, I. A. Popov, G. V. Lopez, X. Chen, A. I. Boldyrev, J. Li and L. S. Wang, *J. Chem. Phys.*, 2016, **144**, 154310.
- 29 Y. J. Wang, Y. F. Zhao, W. L. Li, T. Jian, Q. Chen, X. R. You, T. Ou, X. Y. Zhao, H. J. Zhai, S. D. Li, J. Li and L. S. Wang, *J. Chem. Phys.*, 2016, **144**, 064307.
- 30 H. R. Li, T. Jian, C. Q. Miao, Y. J. Wang, Q. Chen, X. M. Luo, K. Wang, H. J. Zhai, S. D. Li and L. S. Wang, *Phys. Chem. Chem. Phys.*, 2016, **18**, 29147.
- 31 W. L. Li, R. Pal, Z. A. Piazza, X. C. Zeng and L. S. Wang, *J. Chem. Phys.*, 2015, **142**, 204305.
- 32 T. B. Tai and M. T. Nguyen, *Chem. Commun.*, 2016, **52**, 1653.
- 33 S. X. Li, Z. P. Zhang, Z. W. Long and S. J. Qin, *Sci. Rep.*, 2017, **7**, 40081.
- 34 T. B. Tai and M. T. Nguyen, *RSC Adv.*, 2017, **7**, 22243.
- 35 T. B. Tai and M. T. Nguyen, *Chem. Commun.*, 2015, **51**, 7677.
- 36 S. G. Xu, Y. J. Zhao, J. H. Liao and X. B. Yang, *J. Chem. Phys.*, 2015, **142**, 214307.
- 37 N. Karmodak and E. D. Jemmis, *Chem.-Asian J.*, 2016, **11**, 3350.
- 38 H. L. Dong, B. Lin, K. Gilmore, T. J. Hou, S. T. Lee and Y. Y. Li, *Curr. Appl. Phys.*, 2015, **15**, 1084.
- 39 R. X. He and X. C. Zeng, *Chem. Commun.*, 2015, **51**, 3185.
- 40 S. X. Li, Z. P. Zhang, Z. W. Long, G. Y. Sun and S. J. Qin, *Sci. Rep.*, 2016, **6**, 25020.
- 41 S. Bosi, R. T. Da, G. Spalluto and M. Prato, *Eur. J. Med. Chem.*, 2003, **38**, 913.
- 42 R. Bakry, R. M. Vallant, M. Najam-ul-Haq, M. Rainer, Z. Szabo, C. W. Huck and G. K. Bonn, *Int. J. Nanomed.*, 2007, **2**, 639.
- 43 P. W. M. Blom, V. D. Mihailetchi, L. J. A. Koster and D. E. Markov, *Adv. Mater.*, 2007, **19**, 1551.
- 44 B. Liu, R. Q. Png, L. H. Zhao, L. L. Chua, R. H. Friend and P. K. Ho, *Nat. Commun.*, 2012, **3**, 1321.
- 45 V. Buntar and H. W. Weber, *Supercond. Sci. Technol.*, 1996, **9**, 599.
- 46 Y. Chai, T. Guo, C. M. Jin, R. E. Haufler, L. P. F. Chibante, J. Fure, L. H. Wang, J. M. Alford and R. E. Smalley, *J. Phys. Chem.*, 1991, **95**, 7564.
- 47 D. S. Bethune, R. D. Johnson, J. R. Salem, M. S. Vries and C. S. Yannoni, *Nature*, 1993, **366**, 123.
- 48 T. Hirata, R. Hatakeyama, T. Mieno and N. Sato, *J. Vac. Sci. Technol.*, A, 1996, **14**, 615.
- 49 M. N. Chaur, F. Melin, A. L. Ortiz and L. Echegoyen, *Angew. Chem., Int. Ed.*, 2009, **48**, 7514.
- 50 H. Bai, Q. Chen, H. J. Zhai and S. D. Li, *Angew. Chem., Int. Ed.*, 2015, **54**, 941.
- 51 P. Jin, Q. H. Hou, C. C. Tang and Z. F. Chen, *Theor. Chem. Acc.*, 2015, **134**, 13.
- 52 W. Fa, S. Chen, S. Pande and X. C. Zeng, *J. Phys. Chem. A*, 2015, **119**, 11208.
- 53 Q. Chen, T. Gao, W. J. Tian, H. Bai, S. Y. Zhang, H. R. Li, C. Q. Miao, Y. W. Mu, H. G. Lu, H. J. Zhai and S. D. Li, *Phys. Chem. Chem. Phys.*, 2015, **17**, 19690.
- 54 Q. Chen, H. R. Li, C. Q. Miao, Y. J. Wang, H. G. Lu, Y. W. Mu, G. M. Ren, H. J. Zhai and S. D. Li, *Phys. Chem. Chem. Phys.*, 2016, **18**, 11610.
- 55 Q. Chen, H. R. Li, W. J. Tian, H. G. Lu, H. J. Zhai and S. D. Li, *Phys. Chem. Chem. Phys.*, 2016, **18**, 14186.
- 56 W. J. Tian, Q. Chen, H. R. Li, M. Yan, Y. W. Mu, H. G. Lu, H. J. Zhai and S. D. Li, *Phys. Chem. Chem. Phys.*, 2016, **18**, 9922.
- 57 P. Jin, L. Yang, C. Liu, Q. H. Hou and L. L. Li, *Theor. Chem. Acc.*, 2017, **136**, 56.
- 58 W. Wang, Y. D. Guo and X. H. Yan, *RSC Adv.*, 2016, **6**, 40155.
- 59 Y. P. An, M. J. Zhang, D. P. Wu, Z. M. Fu, T. T. Wang and C. X. Xia, *Phys. Chem. Chem. Phys.*, 2016, **18**, 12024.
- 60 Z. Yang, Y. L. Ji, G. Q. Lan, L. C. Xu, X. G. Liu and B. S. Xu, *Solid State Commun.*, 2015, **217**, 38.
- 61 M. Moradi, Z. Bagheri and A. Bodaghi, *Phys. E*, 2017, **89**, 148.
- 62 M. Moradi, V. Vahabi and A. Bodaghi, *J. Mol. Liq.*, 2016, **223**, 315.



- 63 Y. Noguchi, O. Sugino, H. Okada and Y. Matsuo, *J. Phys. Chem. C*, 2013, **117**, 15362.
- 64 R. Bauernschmitt and R. Ahlrichs, *Chem. Phys. Lett.*, 1996, **256**, 454.
- 65 M. J. Frisch, *et al.*, *Gaussian 09, Revision A.02*, Gaussian Inc., Wallingford, CT, 2009.
- 66 Q. Chen, S. Y. Zhang, H. Bai, W. J. Tian, T. Gao, H. R. Li, C. Q. Miao, Y. W. Mu, H. G. Lu, H. J. Zhai and S. D. Li, *Angew. Chem., Int. Ed.*, 2015, **54**, 8160.
- 67 Y. Bai, X. Y. Zhao, T. W. Li, Z. L. Lv, S. J. Lv, H. Han, Y. F. Yin and H. Wang, *Carbon*, 2014, **78**, 70.
- 68 D. Porezag and M. R. Pederson, *Phys. Rev. B: Condens. Matter Mater. Phys.*, 1996, **54**, 7830.

